Original Article

Characterization of a novel maraging steel for laser-based powder bed fusion: optimization of process parameters and post heat treatments

Niki Nouri [a,*], Qing Li [a,b], James Damon [a], Fabian Mühl [a], Gregor Graf [b], Stefan Dietrich [a], Volker Schulze [a]

[a] Institute for Applied Materials — Materials Science and Engineering (IAM-WK), Karlsruhe Institute of Technology, Karlsruhe, Germany
[b] Rosswag GmbH, August-Roßwag-Straße 1, 76327, Pfinztal, Germany

ARTICLE INFO

ABSTRACT

A novel maraging steel with vanadium supplement called Specialis® has been developed for additive manufacturing by powder bed fusion using a laser beam. This study characterized this material after processing and post-processing. An intensive process optimization was carried out by means of a single track melt pool analysis to investigate optimal parameter sets for manufacturing of dense parts. Furthermore, the development of post heat treatment strategies and their influence on mechanical and microstructural characteristics of the material was evaluated. Two main concepts of direct aging treatment (AT) and solution treatment followed by aging treatment (ST+AT) were tested by dilatometry, to analyse the material behaviour with different initial microstructures: as-built and recrystallized. Both heat treatments resulted in a considerable improvement of hardness after only 2 h of aging, increasing to approximately 700 HV and 760 HV respectively, which exceeded the peak hardness of commonly known maraging steel 18Ni300 (660 HV after 6 h). These results were confirmed by tensile tests, where a tensile strength of more than 2300 MPa was achieved. Alongside the precipitation hardening known for maraging steels, the increased hardness was a result of grain refinement due to the addition of vanadium.

1. Introduction

1.1. Laser-based powder bed fusion (PBF-LB)

Due to the increase in component complexity and the growing demand for lightweight design, additive manufacturing (AM) has developed into a highly demanded fabrication process in the last few years. Powder bed fusion (PBF) is a subcategory of this processing method, in which either a laser or an electron beam is used as the heating source to produce metallic parts [1]. Laser-based powder bed fusion (PBF-LB) is a commonly used technology in the PBF field, during which the metal powder is melted by a laser beam, creating the components layer by layer after solidification [2]. Characterization of the melt pool dimensions during PBF processes is an established

method to adapt the solidification structure and optimize the manufactured part [3]. Widely used alloys for PBF-LB are based on iron, nickel, titanium, aluminium and copper.

1.2. PBF-LB of maraging steels

Maraging steels are low-carbon high-strength steels with a ductile, Ni-rich martensitic matrix. The C-Grade maraging steels usually contain about 18 weight-% Ni and the alloying elements Co, Mo, Ti [4]. The ideal characteristics of these steels combine a very high tensile strength and good fracture toughness, complemented by an elevated high-temperature strength, which makes them good candidates in aerospace and tooling applications [5]. To achieve these properties, the established heat treatment of maraging steels consists of two steps: a solution treatment at ~820 °C, followed by the aging treatment in the range of approximately 480 °C—540 °C [6]. The hardening effect is caused by the precipitation of intermetallic phases - such as Ni_3Mo [7,8], η-Ni_3Ti [9,10], Fe_7Mo_6 [9] and Fe_2Mo [10,11] - during aging.

In the past decade, maraging steels of the C-300 grade have become of great interest as a suitable material for PBF-LB. The mechanical characteristics of maraging steels have a positive correlation with part density [12], which is why a number of researchers have studied the influence of process parameters on the density of PBF-LB samples [13—18]. Once the optimal process parameters were studied, the influence of heat treatments and their parameters on the microstructure and mechanical properties were investigated [13,16,17,19—22]. Hardness values of ~660 HV were achieved by either direct-ageing or aging after solution treatment, both after 6 h between 480 °C and 520 °C. This indicates that the PBF-LB microstructures can achieve similar hardness levels as conventionally manufactured maraging steel. Comparative studies [23,24] have shown that age hardening effects were observed in both heat treated conventionally manufactured maraging steel and heat treated PBF-LB maraging steel. However, specific optimisations are needed to reach peak hardness. Studies on the precipitation reactions in PBF-LB maraging steel have not observed any intermetallic precipitation in the as-built samples, but in heat treated samples [25,26]. Nevertheless, tailored intrinsic heat treatments during the PBF-LB process may potentially lead to sufficient age hardening and thereby enable the waiver of post-heat treatments [27,28].

1.3. This work

New manufacturing conditions are one of the reasons for reconsideration of alloy designs, hence optimization approaches exist for PBF-LB alloys. As a promising material for AM, it is advantageous to improve the chemical composition

of maraging steels to obtain enhanced properties than those known from the commonly used C-300 grade. A novel tool steel alloy composition for PBF-LB fabrication was developed by SpecMaterials and qualified by Rosswag Engineering [29]. The composition of this material, Specialis®, was based on 18Ni300 (also X3NiCoMoTi18-9-5 or 1.2709) [30] and 18Ni350 (also X2NiCoMoTi18-12-4 or 1.6356) [30]. As a supplement, a considerable amount of vanadium (1.5 weight-%) was added. The first maraging steels containing vanadium were studied in the 1960s [31], yet vanadium never belonged to the commonly used composition of maraging steels, and Specialis® is a new attempt to develop a vanadium-containing maraging steel suitable for PBF-LB.

Previously [29] a material with similar chemical composition underwent first examinations regarding processing and heat treatment, but microcracking issues due to thermally induced local stresses [32] were still to be addressed. Therefore a new batch of this material powder was produced after a readjustment in the chemical composition by reducing the amount of Al, C, Co and Ti. This study aims to investigate a suitable PBF-LB process window and resulting mechanical properties of the novel maraging steel regarding applicable post heat treatments. Firstly, different parameters of the PBF-LB process were varied and the resulting melt pool geometry and porosity were studied to define the optimal process window. Secondly, the impact of various heat treatments, derived from the common maraging steel heat treatment, on hardness and tensile strength were investigated. Microstructures were analysed at different stages by X-ray diffraction and light optical microscopy.

2. Experimental

2.1. Material

The chemical composition of the investigated material Specialis® is shown in Table 1, alongside those of PBF-LB 18Ni300 and conventionally manufactured 18Ni350 for comparison.

The particle size distribution of the argon atomized Specialis® powder, measured by Rosswag Engineering, had a median of 31 μm, as well as d_{10} and d_{90} values of respectively 19 μm and 52 μm. Furthermore, the bulk density of the material, determined on a cast sample, was $\rho_b = 7.96$ g/cm^3.

2.2. Process parameters

2.2.1. Single track melt pool analysis

The investigations of Specialis® were carried out on samples manufactured with the metal PBF-LB machine SLM 280 HL by SLM Solutions. To determine a suitable set of process parameters for the material, an extensive Design of Experiment

Table 1 – Chemical composition of the investigated material (weight-%).								
Material	C	Ni	Co	Mo	Ti	V	Al	Fe
Specialis®	0.02	18.33	11.39	4.44	1.75	1.54	0.38	Bal.
18Ni300 PBF-LB	0.02	17.72	9.33	4.37	0.90	0.04	0.02	Bal.
18Ni350 conv.	0.01	18.41	12.40	4.99	1.51	0.01	0.11	Bal.

(DoE) with different parameter sets was investigated. Since the evaluation of 3D parts requires complex measurements of porosity, a study of single track melt pools was carried out as a first evaluation step. Two main parameters were varied: laser power, P, ranging between 50 W and 350 W, and scan speed, υ, ranging between 250 mm/s and 1800 mm/s, leading to over 450 different melt pools. The single tracks were created on top of Specialis® base samples printed with the following standard parameters, known from the printing of 18Ni300: 200 W laser power and 800 mm/s scan speed. The layer thickness was set to 30 μm with a hatch spacing of 120 μm. The gas atmosphere and building plate were at room temperature.

Regarding the specific dimensions of the melt pool shown in Fig. 1 (depth D and width W), as well as their relation to the layer thickness T, the examined melt pools were divided into four categories [33–35]: keyhole, under-melt, balling and regular. A keyhole geometry is characterized by an excessively deep melt pool, whereas the under-melt melt pool is not deep enough to remelt the underlying layer, which may result in a lack of fusion defect. Balling typically consists of spheric caps above the base plate which create undercuts in the melt pool. For the analysis of the melt pool, following geometrical definitions were set using image analysis based on previously mentioned sources: keyhole is defined by condition $D/T > 3.5$, whereas melt pools with a ratio of $D < T$ are categorized as under-melt. Furthermore, all melt pools that met condition $1.5 < D/T < 3.5$ were favourable and selected as regular. Balling effect doesn't undergo a geometrical definition as its typical shape is sufficient to identify the melt pool.

In addition, a statistical analysis was carried out to verify correlation between the laser parameters and melt pool geometries by determining the linear fit between different combinations of process parameters and melt pool dimensions.

2.2.2. Transferability to bulk samples

Many boundary conditions, such as heat flow, are not comparable between a single track melt pool and a melt pool in a 3D part. For this reason, the suitability of a selected parameter set, chosen after the single track melt pool analysis, should be verified on a PBF-LB bulk sample. Since the geometry of the melt pool within a part is difficult to determine due to the variation of scanning patterns during manufacturing, porosity was used as a quality factor. Bulk samples were created with the following parameter sets, which led to regular single track melt pools: laser powers of 180 W and 200 W, as well as a scan
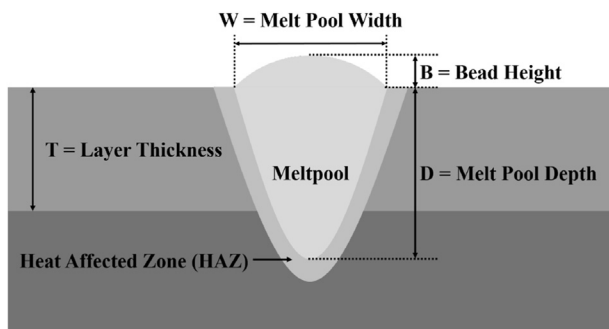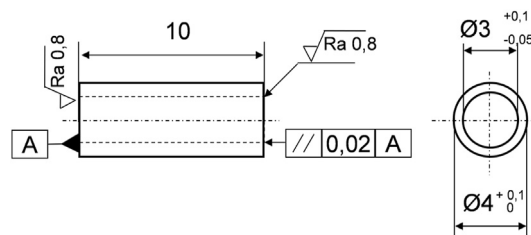

Fig. 2 – **Geometry of the dilatometer samples (dimensions in mm).**

speeds of 720 mm/s, 800 mm/s and 880 mm/s. The scan direction of the laser was rotated by 67° for each new layer. The porosity of these 6 bulk samples was measured by 2D micrograph analysis (Section 2.3.1) to verify the transferability of a suitable parameter set for single tracks to PBF-LB samples. As a verification, bulk samples created with 200 W and 800 mm/s also underwent a series of Archimedes' density measurements.

2.3. Methods

2.3.1. Determination of porosity

Two methods were used for the measurement of porosity. A 2D micrograph analysis was carried out on cubic bulk samples with 1 cm³ volume, using ImageJ [36] to determine the porosity of polished samples. Varying the captured region, nine micrographs with a magnification of 100 ×, corresponding to a surface of approximately 1.36 mm × 1.03 mm, were taken from each sample. The porosity analysis was carried out in three different depth ranges for better statistics, resulting in a sum of 27 images per sample for porosity analysis. Furthermore, the densities of PBF-LB Specialis® cylinders formed from sections of the specimens used for the tensile test were measured using the Archimedes' method. A Density Kit ME-DNY-43 precision balance from Mettler Toledo with 0.1 mg readability was used to measure the weight of the sample in air m_{air} and in distilled water m_{water}, as well as the density of the distilled water ρ_{H_2O}. The density of the sample ρ was measured using Eq. (1).

$$\rho = \frac{m_{air}}{m_{air} - m_{water}} \rho_{H_2O} \tag{1}$$

The relative density of the material was calculated from

$$\rho_{rel} = \rho / \rho_b \tag{2}$$

where ρ_b is the bulk density of a cast sample.

2.3.2. Post heat treatment

A DIL 805 dilatometer (TA Instruments) was used to perform all post heat treatment experiments to enable a precise control of time and temperature. The inductive heating took place in a vacuum chamber, flooded with helium, to avoid any oxidation or evaporation. Temperature was controlled using a thermocouple type S, which was spot welded on the centre of the cylindrical hollow sample with a length of 10 mm, shown in Fig. 2. The samples were fabricated at room temperature with the verified standard process parameter set (Section 2.2.1 and 2.2.2) of 200 W laser power, 800 mm/s
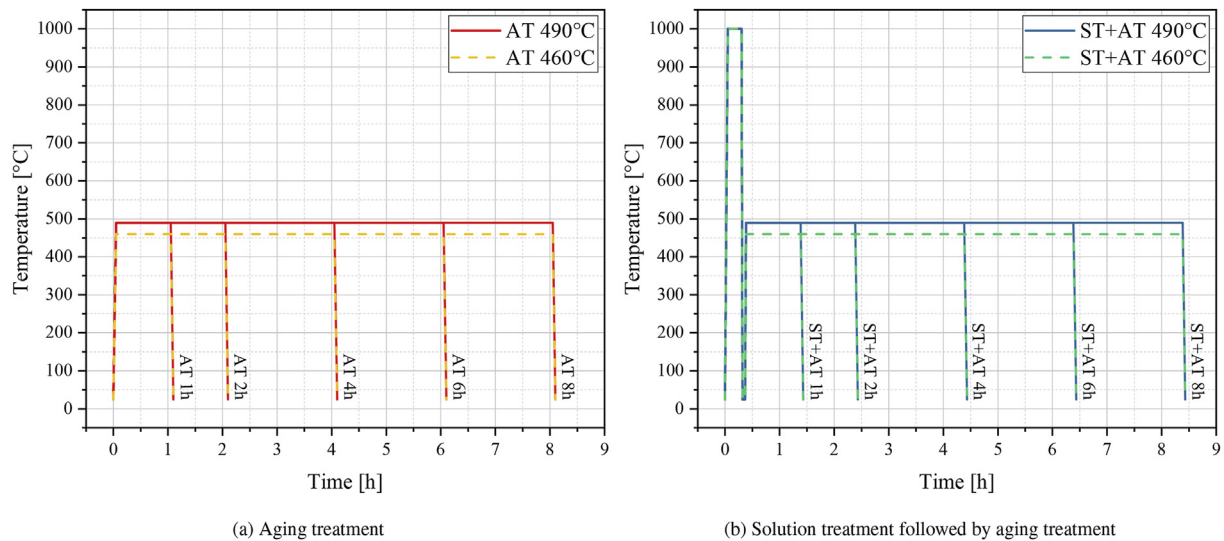

Fig. 1 – **Geometry of an PBF-LB single track melt pool and its significant dimensions.**

(a) Aging treatment   (b) Solution treatment followed by aging treatment

Fig. 3 − Temperature profiles for a) AT and b) ST+AT heat treatments.

scan speed, 30 μm layer thickness, 120 μm hatch spacing and 67° rotation of scan direction for each new layer. Effects due to boundary parameters were excluded by machining of the surfaces.

Investigated heat treatments were divided into three groups. The solution treated samples (ST) were heated to the solution treatment temperature T_S within 3 min; they were quenched to room temperature with helium after holding for 15 min, which was sufficient to eradicate the solidification microstructure. The aged samples (AT) were heated to the aging temperature $T_A = 460\,°C$ or $T_A = 490\,°C$ with a heating rate of 100 °C/s. After holding at temperature for the aging time t_A between 1 and 8 h, the samples were cooled to room temperature at a rate of 100 °C/s, using helium. Both heat treatments were successively carried out on the solution treated and aged samples (ST+AT). The solution treatment of ST+AT samples was carried out at $T_S = 1000\,°C$. The temperature profiles for these heat treatments including the variation of T_A and t_A are shown in Fig. 3.

2.3.3. Microstructural characterization

The amount of γ phase was determined by X-ray diffraction (XRD) with a Bruker D2 Phaser using Cu K_α radiation. The scans were done in a 2θ range from 48° to 105° with a step size of 0.01°. The data evaluation was carried out using a 6-line-method according to ASTM E975 [37] by calculating the integrated intensity of each diffraction peak (hkl). The {200}, {220}

and {311} diffraction peaks were used for austenite and the {200}, {211} and {220} diffraction peaks for martensite.

For the metallographic analysis, each dilatometer sample was cut in the middle, perpendicular to the axial direction and one half was cold embedded for further analysis of the cross section. After grinding and polishing, the samples were etched in 2% Nital. A light optical microscope was used to investigate the microstructures.

2.3.4. Mechanical characterization

Measurements of the Vickers hardness were carried out at $HV_{0.1}$ due to the small cross-sectional area, using a Qness Q30a + micro-hardness tester according to the standard DIN EN ISO 6507-1 [38]. The mean value was calculated from a minimum of 27 indentations.

Tensile tests were performed at room temperature according to the standard DIN EN ISO 6892-1 [39] with a strain rate of 0.0067 1/s on a Zwick Roell Zmart.Pro 200 kN machine with the automated extensometer MultiExtense. Fig. 4 shows the tensile test sample geometry with a coefficient of proportionality $k = 11.3$, which corresponds to the original gauge length L_0 divided by the root of original cross-sectional area $\sqrt{S_0}$. These samples were fabricated using the same parameter set as the dilatometer samples (Section 2.3.2). The experiments were carried out for three different conditions: AT 490 °C 2 h, ST+AT 490 °C 2 h and ST+AT 490 °C 8 h. Each condition was tested using a minimum of 3 samples.
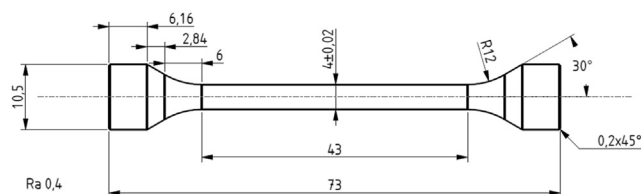
3. Results and discussion

3.1. Evaluation of process parameters

3.1.1. Melt pool analysis

The melt pool geometries were analysed and divided into the four categories described in Section 2.2.1. The result is shown in Fig. 5, where each data point represents a parameter set. The
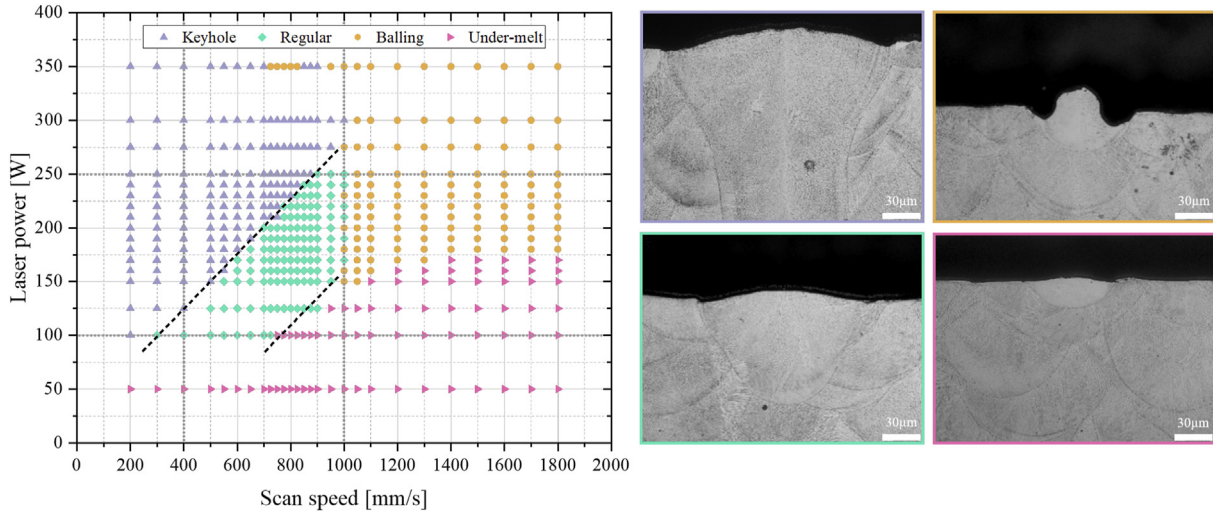

Fig. 4 − Geometry of the tensile test samples in accordance with DIN EN ISO 6892-1 [39] (dimensions in mm).

Fig. 5 — Result of the single track melt pool analysis, showing the relation between parameter sets and the corresponding melt pool geometry. The green points represent suitable parameter sets, which create a normal and regular single track melt pool. Gray lines divide the parameters leading to regular meltpool from those which lead to irregular ones. Black lines approximately represent the linear function dividing the regular melt pool from keyhole and undermelt melt pools.

melt pool dimensions generally increased with decreasing scan speed or increasing laser power. Thus, deep keyhole melt pools are in the left upper corner of the diagram, while the under-melt category is located in the lower right side. In addition, the combination of high laser power (> 175 W) and high scan speed (> 1000 mm/s) always resulted in the balling effect. Other than a few exceptions, laser powers below 100 W or above 250 W and scan speeds below 400 mm/s or above 1000 mm/s led to irregular melt pools (borders are shown with gray lines in Fig. 5). Nevertheless, the build rate could be raised by increasing the scan speed up to 1000 mm/s instead of 800 mm/s, which was used for this material (Section 2.2.1).

3.1.2. Statistical correlations

The general trend in Fig. 5 shows that a linear relation between laser power and scan speed defines the borders (marked with black lines) separating regular melt pools from

keyhole and under-melt, which are defined based on their depth. This confirms that the ratio between laser power and scan speed had a direct influence on the dimensions of the melt pool. Therefore, a statistical verification was carried out, as mentioned in Section 2.2.1, where following significant relations could be expected: width $W \propto \sqrt{P/v}$ [40] and depth $D \propto P/v$ [41]. The results of the statistical analysis showed that these ratios are also valid for Specialis®. Fig. 6 visualizes these correlations and their corresponding Pearson correlation coefficient R. Thus, the combination of the parameters laser power and scan speed must be carefully chosen, as they directly have an impact on the resulting melt pool geometry.

3.1.3. Transferability to bulk samples

As mentioned in Section 2.2.2, the impact of process parameters on the PBF-LB structure had to be studied on bulk samples after the single track melt pool analysis, to verify the
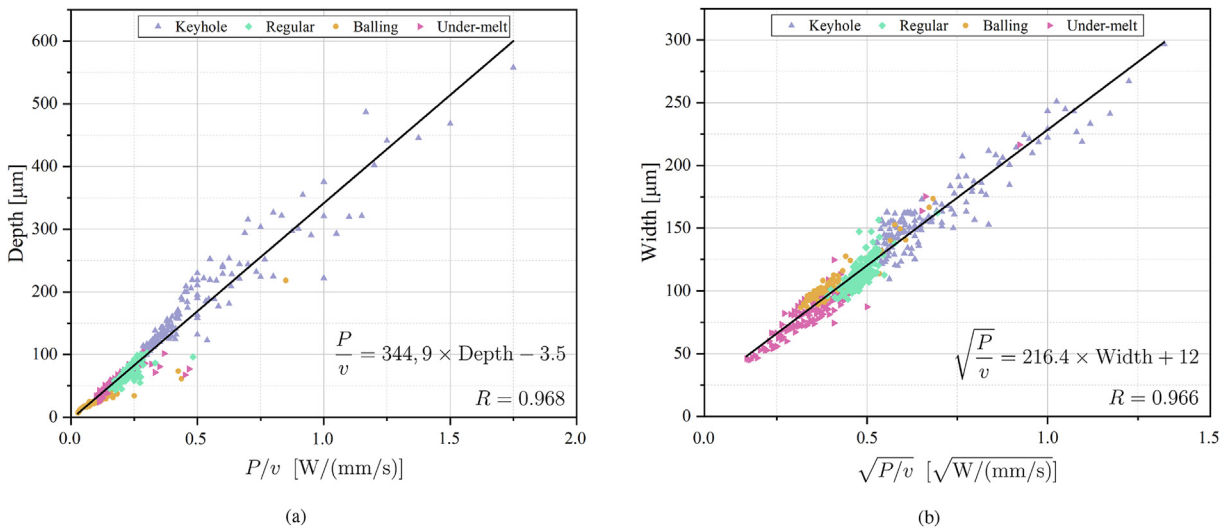

(a)

(b)

Fig. 6 — Correlation between laser parameters (power and scan speed) and melt pool geometry (depth and width).

(a) Aging treatment

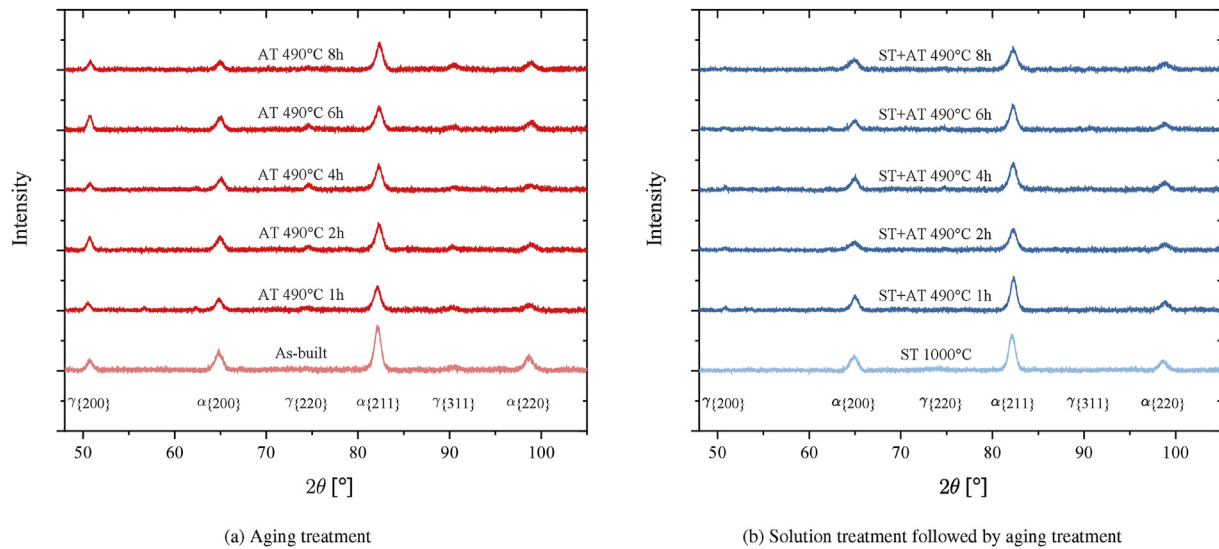(b) Solution treatment followed by aging treatment

Fig. 7 — The XRD diffractograms in dependence of the heat treatment state.

transferability of the results. Thus, the density of bulk samples fabricated with six independent parameter sets, which created regular melt pools were studied using two different measurement methods. It was suggested for 316L steel [42] that measured values by 2D micrograph analysis were systematically higher than those from Archimedes' method in high density areas. The deviation of porosity by 2D micrograph analysis is due to a limited investigated layer of the bulk sample. Therefore Archimedes' method, if carried out correctly, may provide a more reliable result [43]. On the other hand, the 2D micrograph analysis enables the observation of pore geometries and dimensions. Nevertheless, it has also been shown for Ti6Al4V [44] and AlSi10Mg [45] that both methods led to a similar trend with consistent results. For this study, the elaborated transferability from regular melt pools in single tracks to melt pools in bulk PBF-LB parts showed promising outcomes for both measurement methods. The 2D micrograph analysis resulted in a relative density of $\rho_{rel,2D-} = 99.76 \pm 0.1\%$, whereas that calculated by the Archimedes' method was $\rho_{rel,Ar} = 99.74 \pm 0.4\%$. The single track melt pool analysis has been shown to be a suitable method for the evaluation of laser parameters, as both porosity results (2D micrograph and Archimedes') indicated very stable and low defect concentrations. The described methodology [33] bypasses the necessity of printing a large number of bulk samples and investigating their porosity and microstructural characterization, which saves time and cost.

3.2. Microstructure development

3.2.1. Retained/reverted austenite
During the precipitation sequence of aging, an enrichment of the maraging steel matrix with nickel and consequently an increase in austenite ("reverted" austenite) occurs [25]. In the diffractograms in Fig. 7 the AT samples have higher γ peaks than ST+AT samples. Further analysis was carried out, as mentioned in Section 2.3.3, to determine the amount of austenite.

Fig. 8 shows the results of austenite analysis with aging time for Specialis®. As-built samples contained about 10% retained austenite, which is more than the amount that could be achieved for as-built PBF-LB 18Ni300 [13,21−23,46]. This could be attributed to the low martensite finish temperature of this material, which could not be reached in preliminary tests, during which a dilatometer sample was solution treated and then cooled to room temperature. Hence, a fully martensitic structure could not be created during the PBF-LB process, as cooling below room temperature was not possible in this experimental set-up. During aging the austenite content rose significantly up to $17 \pm 3.98\%$ after 2 h and remained almost constant over the entire aging time up to 8 h with a mean value of 18.84%, as a result of reverted austenite formation.
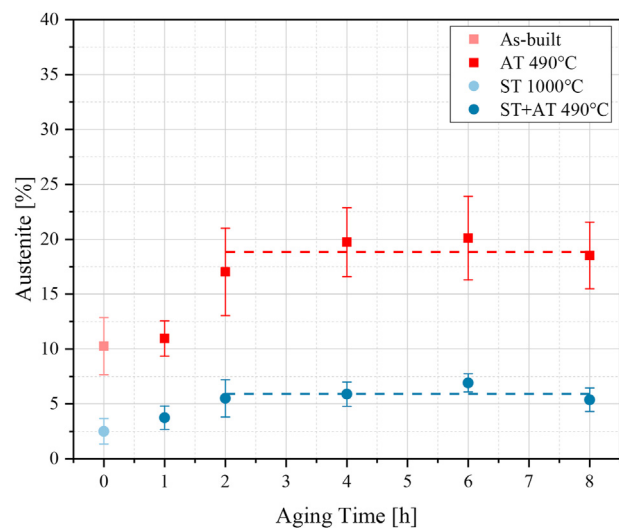

Fig. 8 — Development of austenite content of Specialis®, determined with the 6-line-method according to ASTM E975 [37], after AT and ST+AT. In both cases, a plateau is reached after 2 h of aging (represented by the dashed lines).
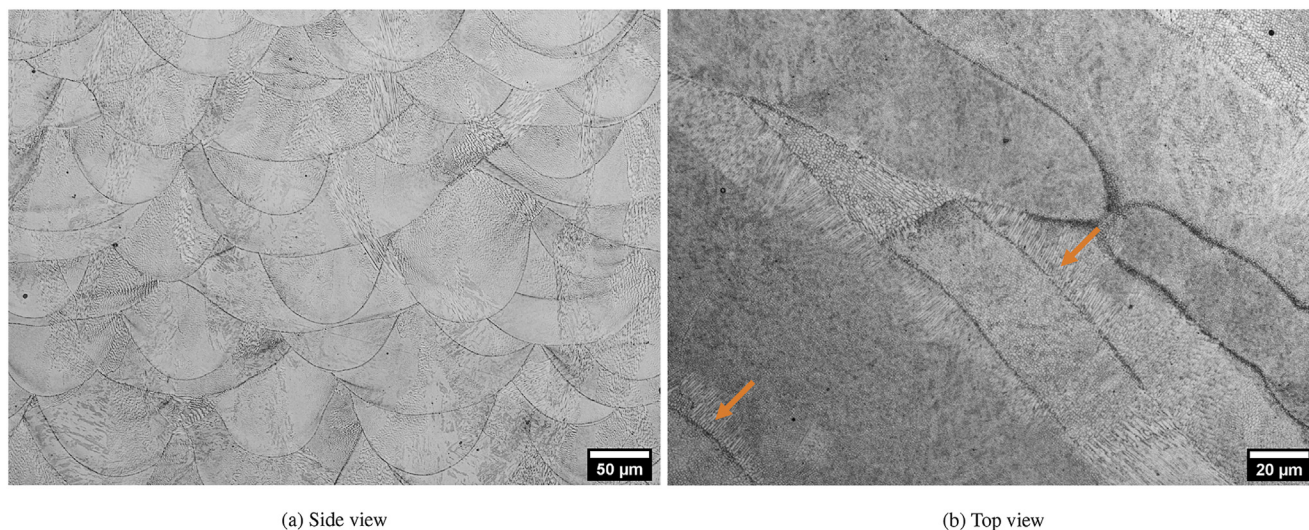
(a) Side view

(b) Top view

Fig. 9 — Optical micrographs showing the as-built microstructure of Specialis®.

Additionally, the segregation of Ni at grain boundaries during aging was a probable cause for this increase, as Ni acts as an austenite stabilizer [47]. Other studies also reported an increase of austenite amount after aging [13,16,19,21—23]. Furthermore, the austenite amount of the ST sample considerably decreased to below 3%, possibly as segregation and chemical inhomogeneities were all eradicated during the solution treatment. Nevertheless, the austenite content increased to approximately 5%—7% during aging due to austenite reversion and Ni-segregation at grain boundaries.

3.2.2. Microscopy

The as-built microstructure is shown in Fig. 9. PBF-LB laser tracks were clearly visible from the side (Fig. 9a) and from the top (Fig. 9b). A cellular structure was formed alongside columns (marked with orange arrows) perpendicular to laser track boundaries. This fine martensitic structure was observed in PBF-LB 18Ni300 Maraging steel [48]. The complex thermal cycle of AM, consisting of fast solidification and high temperature gradients leads to the fine microstructures [49]. The ratio between temperature gradient and growth rate determines the final structure [50]. It was assumed that the high heat input as a result of small radial distance from the laser beam centre leads to the evenly formed cellular structure in the middle of laser tracks [20]. Additionally, the degree of under-cooling decreases at the laser track boundaries due to the thermal heat flow from the centre to the margins. This could prevent the nucleation of new grains, yet the high crystal growth rate leads to the columnar growth of fine structures in the thermal flux direction.

(a) AT, $T_A = 490\,°C$, $t_A = 2\,h$
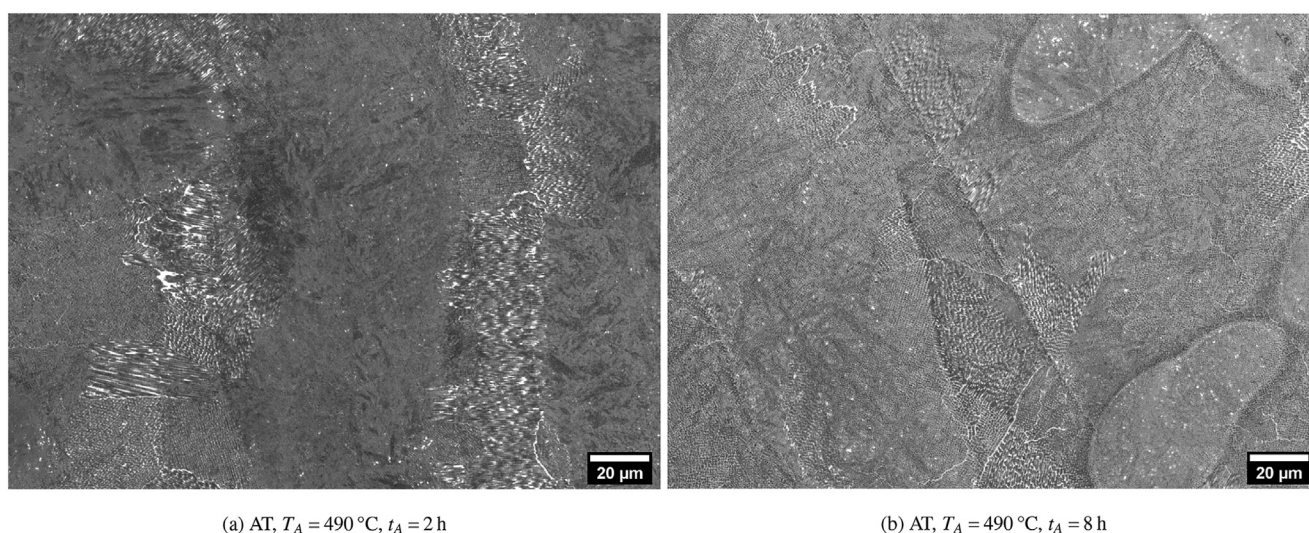
(b) AT, $T_A = 490\,°C$, $t_A = 8\,h$

Fig. 10 — Optical micrographs showing the AT microstructure of Specialis® after different aging times, consisting of PBF-LB solidification structure, nickel martensite matrix and white austenitic areas within melt pool boundaries.

(a) Specialis® ST+AT, $T_A = 490\,°C$, $t_A = 6\,h$ (b) PBF-LB 18Ni300 ST+AT, $T_A = 490\,°C$, $t_A = 6\,h$
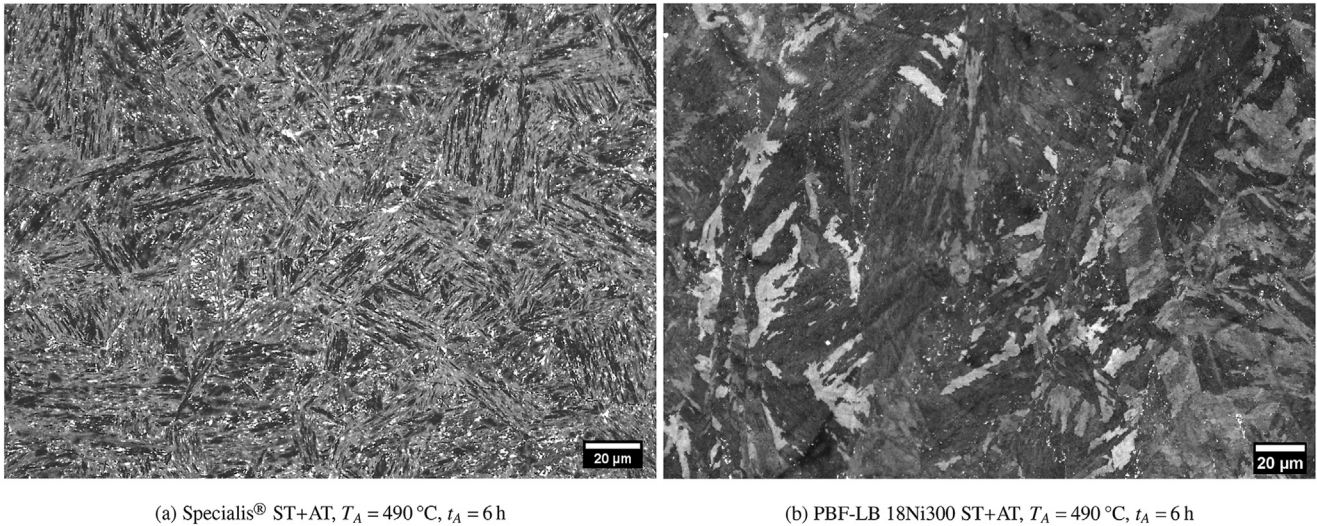
Fig. 11 – Optical micrographs showing the ST+AT microstructure of Specialis® and PBF-LB 18Ni300, consisting of a homogenized nickel martensite matrix and white austenitic areas. The novel composition of Specialis® led to grain refinement in the microstructure.

The microstructure of ST samples showed that after the commonly used solution treatment at $\sim T_S = 815\,°C$, the structure was not yet homogenized and the solidification structure was still visible (similar to Fig. 9), whereas a higher austenitisation temperature of $T_S = 1000\,°C$ eradicated all PBF-LB laser tracks. For this reason, all solution treatments for ST+AT samples were carried out at $T_S = 1000\,°C$.

Fig. 10 gives an overview of microstructures after different aging treatments for the AT samples after 2 h and 8 h of aging at $T_A = 490\,°C$. The laser tracks of PBF-LB were still visible on both AT samples. White austenitic zones were observed within melt pool boundaries, as previously reported [51]. There is no significant difference visible as a result of the variation of aging time t_A.

Contrary to the AT samples, ST+AT heat treatment led to a homogenized fine structure (Fig. 11a), which corresponds to the typical shape of lath martensite with a lower amount of white austenitic areas. As mentioned in Section 3.2.1, AT samples contained approximately 17%–20% γ-phase, which was reduced to about 5%–7% in the ST+AT samples.

A comparison of ST+AT sample to the structure of PBF-LB 18Ni300 (Fig. 11b) showed that Specialis® (Fig. 11a) had a much finer martensite lath and austenite structure than 18Ni300. A possible explanation for the grain refinement was the addition of vanadium. Even small amounts of vanadium result in grain refinement in ferritic-pearlitic micro alloyed structural steels [52], high strength bainitic steels [53] and pure aluminium [54].

3.3. Influence of post heat treatments on mechanical characteristics

3.3.1. Hardness

The development of the hardness of Specialis® depending on the heat treatment and its corresponding aging time t_A and temperature T_A is shown in Fig. 12. As expected, the hardening mechanism known from commonly used maraging steels for PBF-LB [22,24] led to a significant increase of the hardness after both AT and ST+AT. Although the ST sample ($338 \pm 6\,HV_{0.1}$) had a lower hardness than the as-built condition ($370 \pm 10\,HV_{0.1}$), the ST+AT samples obtain a higher hardness value than the directly aged AT samples. The decreased amount of retained austenite after the ST+AT heat treatment was assumed to cause the higher hardness compared to AT heat treatment.

Considering the overlapping error bars, the variation of T_A had no notable effect on the hardness of Specialis Regarding the aging time t_A, the curves show a significant increase in hardness until $t_A = 1\,h$, followed by another increase of
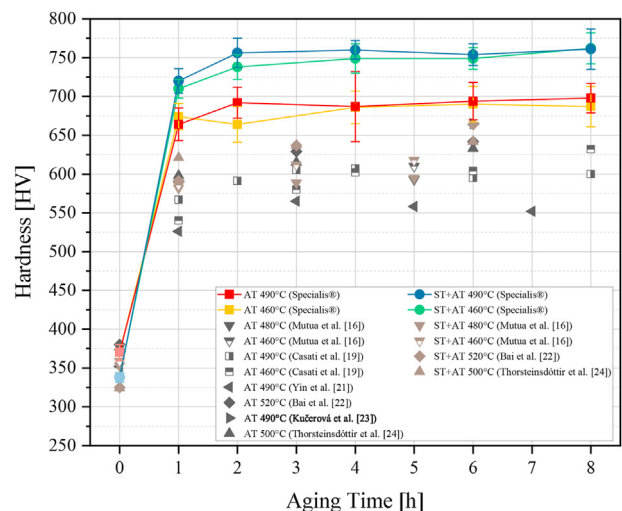

Fig. 12 – Influence of heat treatment parameters on the hardness of Specialis®, with yellow and red curve for AT, as well as green and blue curve for ST+AT. Gray and brown points respectively correspond to AT and ST+AT values for PBF-LB 18Ni300 from literature [16,19,21–24].
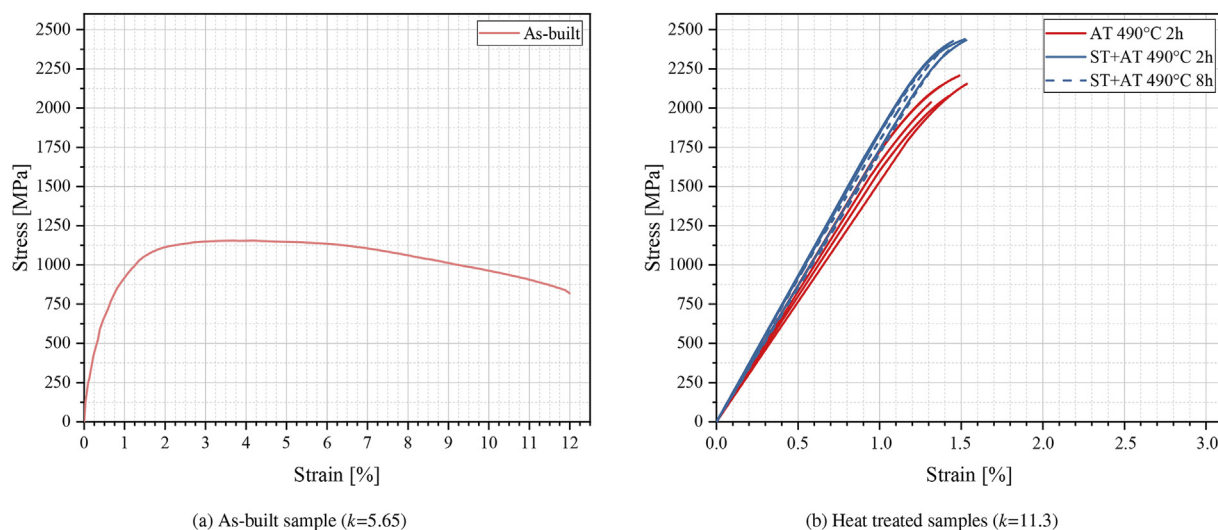
(a) As-built sample ($k=5.65$)

(b) Heat treated samples ($k=11.3$)

Fig. 13 – Strain stress curves of the tensile tests.

approximately 30 $HV_{0.1}$ if aged up to 2 h. The exception of AT 460 °C, which had a decreasing tendency between 1 h and 2 h, was considered to be insignificant due to the overlapping error bars. Both heat treatments at $T_A = 490$ °C led to constant hardness values (difference less than 1%) after 2 h, independent of aging time. The analysis revealed that the age hardening mechanism due to intermetallic precipitations already took place at early aging stages. Thus, considerable time could be saved and costs reduced without compromising on the hardness, by using shorter aging times.

Furthermore, the hardness results of heat treated Specialis® were compared to those of 18Ni300 [16,19,21–24] measured by Vickers hardness. The highest achieved values after AT and ST+AT are depicted in Fig. 12. The hardness of 18Ni300 continuously increased with the aging time up to $t_A = 6$ h. Also, neither of the two heat treatments (AT or ST+AT) invariably led to higher hardness, but it depended on the corresponding T_A and t_A.

The comparison of Specialis® with PBF-LB 18Ni300 [16,19,21–24] showed an increase of at least 35 HV (5%) for AT and 100 HV (15%) for ST+AT in hardness, reaching a peak of 698 ± 19 $HV_{0.1}$ and 762 ± 20 $HV_{0.1}$, respectively. In addition to the known precipitation hardening effect in maraging steels [30], the observed grain refinement (Section 3.2.2) and the associated grain boundary hardening effect due to the Hall–Petch relationship [55] can be assumed to be another significant strengthening mechanisms.

3.3.2. Tensile strength

Fig. 13 shows a comparison of the tensile test results between as-built samples (carried out by Rosswag as reference samples with a coefficient of proportionality $k = 5.65$) and heat treated samples (Section 2.3.4). The as-built sample had a yield strength of $R_{p0.2} = 751 \pm 18$ MPa and a tensile strength of $R_m = 1150 \pm 16$ MPa. The yield strength $R_{p0.2}$ was not evaluable for the heat treated samples, as they all had a very low elongation after fracture $A_{11.3} < 0.2\%$, due to brittle fracture. Similar to the hardness values, the yield strength of ST+AT samples was higher than AT samples due to the different amounts of austenite. The tensile strength of AT samples ($R_m = 2124 \pm 60$ MPa) increased by over 80% after aging. Moreover, ST+AT heat treatment increased the tensile strength by more than 100% compared to the as-built condition, reaching 2433 ± 5 MPa after 2 h and 2338 ± 78 MPa after 8 h. The comparison between ST+AT 490 °C 2 h and ST+AT 490 °C 8 h indicated that the longer aging time slightly decreased the tensile strength. A possible explanation could be the beginning of over-aging at 8 h. Furthermore, the ST+AT samples reached approximately the same tensile strength as conventionally manufactured 18Ni350 ($R_{m,18Ni350} = 2370$ MPa [56]), with a lower total elongation ($A_{t,18Ni350} = 6\%$ [56]).

3.3.3. Overview of heat treatment strategies

In summary, the highest values of mechanical characteristics were achieved with the ST+AT at $T_A = 490$ °C for 2 h (756 ± 19 $HV_{0.1}$, $R_m = 2433 \pm 5$ MPa) and $T_A = 490$ °C for 8 h (762 ± 20 $HV_{0.1}$, $R_m = 2338 \pm 78$ MPa) as a result of precipitation hardening, grain refinement effects and reduced austenite. Nevertheless, AT samples also reached higher values than PBF-LB 18Ni300 after aging at $T_A = 490$ °C for 2 h (698 ± 19 $HV_{0.1}$, $R_m = 2124 \pm 60$ MPa). Depending on the applications' requirements, the components could either be aged directly, or be solution annealed first for increased hardness and strength. Furthermore, the aging treatment could be integrated in the PBF-LB process, if the mechanical characteristics fulfil the demands. A tailored intrinsic AT during the additive manufacturing would optimize the fabrication process, so that a post heat treatment would not be necessary. Therefore, further research on the phase transformations and microstructural development of Specialis® during different heat treatments is recommended, in order to identify the resulting precipitations and their kinetics. Moreover, the possibility of vanadium precipitation and resulting strengthening mechanisms during aging warrants supplementary investigations. This would enable a better understanding of the hardening effects and their origins, as well as the interaction between different precipitations.

4.   Conclusions

A novel maraging steel for AM by PBF-LB, Specialis®, was studied for suitable process parameters. Different heat treatment strategies and their impact on the resulting microstructure and mechanical characteristics were investigated. The following conclusions were drawn:

- The analysis of single track melt pool geometry was used in order to effectively determine suitable laser parameters for the PBF-LB processing of maraging steels. The following linear correlations between melt pool geometry and laser parameters (laser power and scan speed) were verified: width $\propto \sqrt{P/v}$ and depth $\propto P/v$. The selected process parameters, which created a regular melt pool, led to bulk samples with high densities in the range of 99.74—99.76%. This method could minimize the time and cost of the parameter optimization.
- Vanadium supplement to the commonly known chemical composition of maraging steels increased the hardness after heat treatment by grain refinement.
- Specialis® can reach a hardness of $756 \pm 19\,HV_{0.1}$ after solution treatment followed by a suitable aging treatment (ST+AT) at $T_A = 490\,°C$ for 2 h, which is a short aging time compared to the commonly used heat treatment times of maraging steels (6 h). Moreover, the tensile strength exceeded 2370 MPa, which is the maximum value of conventionally manufactured 18Ni350, by reaching 2433 ± 5 MPa.
- Direct aging treatment (AT) leads to lower hardness and tensile strength due to the increasing amount of austenite up to 20%. Nevertheless, high values of $698 \pm 19\,HV_{0.1}$ and $R_m = 2124 \pm 60$ MPa can be achieved.

Fundings

Acknowledgment

REFERENCES

[1] DebRoy T, Wei HL, Zuback JS, Mukherjee T, Elmer JW, Milewski JO, et al. Additive manufacturing of metallic components — process, structure and properties. Prog Mater Sci 2018;92:112—224. https://doi.org/10.1016/j.pmatsci.2017.10.001.

[2] Milewski JO. Additive manufacturing of metals, vol. 258. Cham: Springer International Publishing; 2017, ISBN 978-3-319-58204-7. https://doi.org/10.1007/978-3-319-58205-4.

[3] Soylemez E, Beuth JL, Taminger K. Controlling melt pool dimensions over a wide range of material deposition rates in electron beam additive manufacturing. In: Solid freeform fabrication proceedings, vols. 571—582. Emerald Group Publishing Ltd; 2010.

[4] Floreen S. The physical metallurgy of maraging steels. Metall Rev 1968;13(1):115—28. https://doi.org/10.1179/mtlr.1968.13.1.115. ISSN 0076-6690.

[5] Hall AM, Slunder CJ. Battelle memorial institute, the metallurgy, behavior, and application of the 18-percent nickel maraging steels: a survey, NASA SP, technology utilization division. National Aeronautics and Space Administration; 1968.

[6] Inco Limited. 18 per cent nickel maraging steels: engineering properties. Nickel Development Institute; 1976. 4419.

[7] Spitzig W, Chilton J, Barton C. Structure and strengthening mechanisms in 300-grade 18-Ni-Co-Mo-Ti maraging steel. In: Parina J, editor. Transactions of American society for metals. Metals Park, Ohio: ASM; 1968. p. 635—9.

[8] Decker RF, Floreen S. Maraging steel: the first 30 years. In: Wilson R, editor. Maraging steels: recent developments and applications, the minerals, metals & materials society. Pennsylvania: Warrendale; 1988. p. 1—38.

[9] Sha W, Cerezo A, Smith GDW. Phase chemistry and precipitation reactions in maraging steels: Part I. Introduction and study of Co-containing C-300 steel. Metall Mater Trans 1993;24(6):1221—32. https://doi.org/10.1007/BF02668190. ISSN 1073-5623.

[10] Vasudevan VK, Kim SJ, Wayman CM. Precipitation reactions and strengthening behavior in 18 Wt pct nickel maraging steels. Metall Mater Trans 1990;21(10):2655—68. https://doi.org/10.1007/BF02646061. ISSN 1073-5623.

[11] Lecomte JB, Servant C, Cizeron G. A comparison of the structural evolution occurring during anisothermal or isothermal treatments in the case of nickel and manganese type maraging alloys. J Mater Sci 1985;20(9):3339—52. https://doi.org/10.1007/BF00545204. ISSN 0022-2461.

[12] Casalino G, Campanelli SL, Contuzzi N, Ludovico AD. Experimental investigation and statistical optimisation of the selective laser melting process of a maraging steel. Opt Laser Technol 2015;65:151—8. https://doi.org/10.1016/j.optlastec.2014.07.021. ISSN 00303992.

[13] Kempen K, Yasa E, Thijs L, Kruth J-P, van Humbeeck J. Microstructure and mechanical properties of selective laser melted 18Ni-300 steel. Phys Procedia 2011;12:255—63. https://doi.org/10.1016/j.phpro.2011.03.033. ISSN 18753892.

[14] Hermann Becker T, Dimitrov D. The achievable mechanical properties of SLM produced maraging steel 300 components. Rapid Prototyp J 2016;22(3):487—94. https://doi.org/10.1108/RPJ-08-2014-0096. ISSN 1355-2546.

[15] Bai Y, Yang Y, Wang Di, Zhang M. Influence mechanism of parameters process and mechanical properties evolution mechanism of maraging steel 300 by selective laser melting. Mater Sci Eng, A 2017;703:116—23. https://doi.org/10.1016/j.msea.2017.06.033. 09215093.

[16] Mutua J, Nakata S, Onda T, Chen Z-C. Optimization of selective laser melting parameters and influence of post heat treatment on microstructure and mechanical properties of maraging steel. Mater Des 2018;139(2):486—97. https://doi.org/10.1016/j.matdes.2017.11.042. ISSN 02641275.

[17] Song J, Tang Q, Feng Q, Ma S, Setchi R, Liu Y, et al. Effect of heat treatment on microstructure and mechanical behaviours of 18Ni-300 maraging steel manufactured by selective laser melting. Opt Laser Technol 2019;120(105725). https://doi.org/10.1016/j.optlastec.2019.105725. ISSN 00303992.

[18] Król M, Snopiński P, Czech A. The phase transitions in selective laser-melted 18-NI (300-grade) maraging steel. J

Therm Anal Calorim 2020;142(2):1011—8. https://doi.org/10.1007/s10973-020-09316-4. ISSN 1588-2926.

[19] Casati R, Lemke J, Tuissi A, Vedani M. Aging behaviour and mechanical performance of 18-Ni 300 steel processed by selective laser melting. Metals 2016;6(9):218. https://doi.org/10.3390/met6090218.

[20] Tan C, Zhou K, Ma W, Zhang P, Liu M, Kuang T. Microstructural evolution, nanoprecipitation behavior and mechanical properties of selective laser melted high-performance grade 300 maraging steel. Mater Des 2017;134:23—34. https://doi.org/10.1016/j.matdes.2017.08.026. ISSN 02641275.

[21] Yin S, Chen C, Yan X, Feng X, Jenkins R, O'Reilly P, et al. The influence of aging temperature and aging time on the mechanical and tribological properties of selective laser melted maraging 18Ni-300 steel. Additive Manufacturing 2018;22(3):592—600. https://doi.org/10.1016/j.addma.2018.06.005. ISSN 22148604.

[22] Bai Y, Wang Di, Yang Y, Wang H. Effect of heat treatment on the microstructure and mechanical properties of maraging steel by selective laser melting. Mater Sci Eng, A 2019;760:105—17. https://doi.org/10.1016/j.msea.2019.05.115. ISSN 09215093.

[23] Kučerová L, Zetková I, Jandová A, Bystrianský M. Microstructural characterisation and in-situ straining of additive-manufactured X3NiCoMoTi 18-9-5 maraging steel. Mater Sci Eng: A 2019;750:70—80. https://doi.org/10.1016/j.msea.2019.02.041. ISSN 09215093.

[24] Thorsteinsdóttir EG, Primdahl DS, Zhang YB, Jensen DJ, Yu T. Aging of 3D-printed maraging steel. IOP Conf Ser Mater Sci Eng 2019;580:012047. https://doi.org/10.1088/1757-899X/580/1/012047.

[25] Jägle EA, Choi P-P, van Humbeeck J, Raabe D. Precipitation and austenite reversion behavior of a maraging steel produced by selective laser melting. J Mater Res 2014;29(17):2072—9. https://doi.org/10.1557/jmr.2014.204. ISSN 0884-2914.

[26] Bodziak S, Al-Rubaie KS, Valentina LD, Lafratta FH, Santos EC, Zanatta AM, et al. Precipitation in 300 Grade maraging steel built by selective laser melting: aging at 510 °C for 2 h. Mater Char 2019;151(218):73—83. https://doi.org/10.1016/j.matchar.2019.02.033. ISSN 10445803.

[27] Jägle EA, Sheng Z, Wu L, Lu L, Risse J, Weisheit A, et al. Precipitation reactions in age-hardenable alloys during laser additive manufacturing. J Occup Med 2016;68(3):943—9. https://doi.org/10.1557/jmr.2014.204. ISSN 1047-4838.

[28] Damon J, Koch R, Kaiser D, Graf G, Dietrich S, Schulze V. Process development and impact of intrinsic heat treatment on the mechanical performance of selective laser melted AISI 4140. Addit Manuf 2019;28:275—84. https://doi.org/10.1016/j.addma.2019.05.012. ISSN 22148604.

[29] Nouri N, Dietrich S, Zanger F, Schulze V. Dual-laser PBF-LB processing of a high-performance maraging tool steel FeNiCoMoVTiAl. Materials 2021;14(15):4251. https://doi.org/10.3390/ma14154251.

[30] H. C. ASM International. Metals Handbook: vol. 1: Properties and selection: irons, steels, and high-performance alloys. 10th ed. edn. Materials Park, Ohio: ASM International; 1990, ISBN 978-0-87170-377-4.

[31] Chilton JM, Barton C. Identification of strengthening precipitates in 18Ni(250) aluminium, vanadium, and titanium maraging steel. In: Parina J, editor. Transactions of American society for metals. Metals Park, Ohio: ASM; 1967. p. 528—42.

[32] Harrison NJ, Todd I, Mumtaz K. Reduction of micro-cracking in nickel superalloys processed by selective laser melting: a fundamental alloy design approach. Acta Mater 2015;94:59—68. https://doi.org/10.1016/j.actamat.2015.04.035. ISSN 13596454.

[33] He Y, Zhong M, Beuth J, Webler B. A study of microstructure and cracking behavior of H13 tool steel produced by laser powder bed fusion using single-tracks, multi-track pads, and 3D cubes. J Mater Process Technol 2020;286(116802). https://doi.org/10.1016/j.jmatprotec.2020.116802.

[34] Oliveira JP, LaLonde AD, Ma J. Processing parameters in laser powder bed fusion metal additive manufacturing. Mater Des 2020;193(108762). https://doi.org/10.1016/j.matdes.2020.108762.

[35] Seede R, Shoukr D, Zhang B, Whitt A, Gibbons S, Flater P, et al. An ultra-high strength martensitic steel fabricated using selective laser melting additive manufacturing: densification, microstructure, and mechanical properties. Acta Mater 2020;186:199—214. https://doi.org/10.1016/j.actamat.2019.12.037. ISSN 13596454.

[36] Rasband WS. ImageJ. Bethesda, Maryland, USA: U. S. National Institutes of Health; 1997. URL, https://imagej.nih.gov/ij/.

[37] ASTM International, ASTM E. 975, Practice for X-ray determination of retained austenite in steel with near random crystallographic orientation. 2013. https://doi.org/10.1520/E0975-13.

[38] 10.31030/2778746 Deutsches Institut für Normung, DIN EN ISO 6507-1, Metallische Werkstoffe - Härteprüfung nach Vickers - Teil 1: Prüfverfahren. 2018. 07.

[39] 10.31030/3132591 Deutsches Institut für Normung, DIN EN ISO 6892-1, Metallische Werkstoffe - Zugversuch - Teil 1: Prüfverfahren bei Raumtemperatur. 2020. 06.

[40] Großmann A, Felger J, Frölich T, Gosmann J, Mittelstedt C. Melt pool controlled laser powder bed fusion for customised low-density lattice structures. Mater Des 2019;181(108054). https://doi.org/10.1016/j.matdes.2019.108054.

[41] Suzuki A, Nishida R, Takata N, Kobashi M, Kato M. Design of laser parameters for selectively laser melted maraging steel based on deposited energy density. Addit Manuf 2019;vol. 28:160—8. https://doi.org/10.1016/j.addma.2019.04.018. ISSN 22148604.

[42] de Terris T, Andreau O, Peyre P, Adamski F, Koutiri I, Gorny C, et al. Optimization and comparison of porosity rate measurement methods of selective laser melted metallic parts. Addit Manuf 2019;vol. 28:802—13. https://doi.org/10.1016/j.addma.2019.05.035. ISSN 22148604.

[43] Spierings A, Schneider M, Eggenberger R. Comparison of density measurement techniques for additive manufactured metallic parts. Rapid Prototyp J 2011;17(5):380—6. https://doi.org/10.1108/13552541111156504. ISSN 1355-2546.

[44] Wits WW, Carmignato S, Zanini F, Vaneker TH. Porosity testing methods for the quality assessment of selective laser melted parts. CIRP Annals 2016;65(1):201—4. https://doi.org/10.1016/j.cirp.2016.04.054. ISSN 00078506.

[45] Damon J, Dietrich S, Vollert F, Gibmeier J, Schulze V. Process dependent porosity and the influence of shot peening on porosity morphology regarding selective laser melted AlSi10Mg parts. Addit Manuf 2018;20:77—89. https://doi.org/10.1016/j.addma.2018.01.001. ISSN 22148604.

[46] Conde FF, Escobar JD, Oliveira JP, Béreš M, Jardini AL, Bose WW, et al. Effect of thermal cycling and aging stages on the microstructure and bending strength of a selective laser melted 300-grade maraging steel. Mater Sci Eng, A 2019;758:192—201. https://doi.org/10.1016/j.msea.2019.03.129.

[47] Zhang H, Ji X, Ma D, Tong M, Wang T, Xu B, et al. Effect of aging temperature on the austenite reversion and mechanical properties of a Fe—10Cr—10Ni cryogenic maraging steel. J Mater Res Technol 2021;11:98—111. https://doi.org/10.1016/j.jmrt.2020.12.096. ISSN 2238-7854.

[48] Damon J, Hanemann T, Dietrich S, Graf G, Lang K-H, Schulze V. Orientation dependent fatigue performance and mechanisms of selective laser melted maraging steel

X3NiCoMoTi18-9-5. Int J Fatig 2019;127(5):395—402. https://doi.org/10.1016/j.ijfatigue.2019.06.025. ISSN 01421123.

[49] Herzog D, Seyda V, Wycisk E, Emmelmann C. Additive manufacturing of metals. Acta Mater 2016;117:371—92. https://doi.org/10.1016/j.actamat.2016.07.019. ISSN 13596454.

[50] Kou S. Welding metallurgy. Hoboken, NJ, USA: John Wiley & Sons; 2002, ISBN 0471434914. https://doi.org/10.1002/0471434027.

[51] Jägle EA, Sheng Z, Kürnsteiner P, Ocylok S, Weisheit A, Raabe D. Comparison of maraging steel micro- and nanostructure produced conventionally and by laser additive manufacturing. Materials 2016;10(1). https://doi.org/10.3390/ma10010008.

[52] Lagneborg R, Hutchinson B, Siwecki T, Zajac S. The role of vanadium in microalloyed steels. 2014.

[53] Zajac S. Expanded use of vanadium in new generations of high strength steels. Mater Sci Technol 2006:317—26.

[54] Sun H-p, Wu J, Tang T, Fan B, Tang Z-h. Effect of vanadium carbide on commercial pure aluminum. Intl J Minerals, Metal, and Mater 2017;24(7):833—41. https://doi.org/10.1007/s12613-017-1467-5. ISSN 1674-4799.

[55] Whang SH. Nanostructured metals and alloys: processing, microstructure, mechanical properties and applications. Cambridge: Woodhead Publishing Series in Metals and Surface Engineering Ser, Elsevier Science & Technology; 2011. ISBN: 9780857091123.

[56] Steels for aircraft structures. In: Introduction to aerospace materials. Elsevier; 2012, ISBN 9781855739468. p. 232—50. https://doi.org/10.1533/9780857095152.232.